Computations of a Maneuvering Unmanned Combat Air Vehicle Using a High-Order Overset-Grid Method

Raymond E. Gordnier, Scott E. Sherer, and Miguel R. Visbal
US Air Force Research Laboratory, Air Vehicles Directorate, Computational Sciences Branch (AFRL/VAAC), Wright-Patterson AFB, OH
{raymond.gordnier, scott.shere, miguel.visbal}@wpafb.af.mil

Abstract

Simulating the flow around a maneuvering unmanned combat air vehicle (UCAV) requires a computational method capable of modeling such complex flow features as massive separation, transition from laminar to turbulent flow, and nonlinear vortex dynamics. In the present paper, a parallel, high-order, overset-grid solver is used to compute these challenging flowfields. Turbulence modeling is accomplished using an implicit Large Eddy Simulation (LES) approach, which exploits the characteristics of the sixth-order accurate computational scheme coupled with high-order, low pass filtering. This scheme provides a unified computational approach for the laminar/transitional/turbulent flowfields encountered by maneuvering UCAVs. A general overset-grid capability, including high-order interpolation and the ability to handle holes while maintaining high-order accuracy, has been incorporated into the flow solver. This high-order method is applied to the simulation of a canonical low sweep delta wing and a generic, tailless, low-sweep wing UCAV configuration. Computations performed for the low sweep delta wing at moderate Reynolds numbers demonstrate the ability of the implicit large-eddy simulation (ILES) approach to capture important Reynolds number effects for these complicated transitional flowfields. Groundbreaking high-order computations for the generic UCAV configuration are then presented with the fundamental aerodynamic phenomena of the configuration being examined using the improved accuracy of the high-order overset method. Comparisons with available experimental measurements are made to demonstrate the ability of this high-fidelity modeling approach to capture the complex flow physics involved.

1. Introduction

Unmanned combat air vehicles are playing an increasingly important role in the planning and execution of military operations. The complex flows over these types of maneuvering, unmanned aircraft may involve massive separation whose simulation places numerous demands on a computational method. The flowfields are inherently unsteady and three-dimensional. A combination of laminar, transitional and turbulent flow regions may be present both on the surface of the wing and in the separated vortical flow. The ability to accurately simulate these types of flows and the complicated interactions between the separated vortical flow and the surface boundary layer is vital to capturing key performance coefficients (e.g., pitching moment coefficient, rolling moment coefficient). Therefore, a high degree of fidelity is required to satisfactorily compute these challenging unsteady flowfields.

Traditional Reynolds-averaged Navier-Stokes (RANS) approaches are inadequate to capture even the large-scale temporal dynamics of such complex, unsteady flows, and are also limited in their predictive capabilities for mean flow properties involving separated flows. Recently, Morton, et al.[1,2] and Görtz[3] have investigated the Detached Eddy Simulation (DES) approach for improved prediction of the unsteady, vortical flowfields over delta wings. DES employs a traditional RANS turbulence model (Spallart-Allmaras) to represent the assumed turbulent wall boundary layer. The model then smoothly switches to an LES-like model (Smagorinsky) in the separated region to more accurately represent the separated flow. The DES approach has been implemented into standard second-order accurate flow codes[1,3]. In this paper an alternative implicit LES approach is employed which is based on a sixth-order accurate computational scheme coupled with higher-order, low pass filtering. This scheme is more appropriate for moderate Reynolds numbers where laminar/ transitional flows are encountered.

0-7695-3088-5/07 $25.00 © 2007 IEEE

2. Computational Framework

The computational approach employed in the present work solves the unsteady, three-dimensional Navier-Stokes equations using a well-validated and robust high-order solver (FDL3DI)[4-6]. A number of key features of the FDL3DI code make it most suitable for the present computational challenge. All spatial derivatives are computed through high-order compact or Padé-type[7] difference methods. Schemes ranging from standard 2nd-order to highly accurate 6th-order methods are possible. To enforce numerical stability, which can be compromised by mesh stretching, boundary conditions and non-linear phenomena, a higher-order, low-pass filter is utilized. This discriminating up to 10th-order low-pass filter preserves the overall high-order accuracy of the spatial discretization while retaining stability for nonlinear applications. Careful attention to the treatment of the metric derivatives and the Geometric Conservation Law (GCL)[8] ensures higher-order accuracy on deforming and moving grids.

2.1. Implicit Large Eddy Simulation Methodology

The ILES method to be used in the present computations was first proposed and investigated by Visbal, et al.[9] The underlying idea behind the approach is to capture with high accuracy the resolved part of the turbulent scales while providing for a smooth regularization procedure to dissipate energy at the represented but poorly resolved high wavenumbers of the mesh. In the present computational procedure the 6th-order compact difference scheme provides the high accuracy while the low-pass spatial filters provide the regularization of the unresolved scales. All this is accomplished with no additional sub-grid scale models as in traditional LES approaches. An attractive feature of this filtering ILES approach is that the governing equations and numerical procedure remain the same in all regions of the flow. In addition, the ILES method requires approximately half the computational resources of a standard dynamic Smagorinsky sub-grid scale LES model. This results in a scheme capable of capturing with high-order accuracy the resolved part of the turbulent scales in an extremely efficient and flexible manner.

2.2. Overset Methodology

An overset-grid approach is utilized to provide flexibility for modeling complex geometries. It also serves as a domain decomposition mechanism for application of the high-order approach on massively parallel computing platforms. The first step in this method is to generate overset structured grids based on the physical geometry of the problem. Once the grids are established based on the physical requirements of the problem, the connectivity between them is established using the spatially second-order accurate PEGASUS Version 5 software[10]. Once this grid-level connectivity is established, an in-house pre-processing code named BELLERO[11] is executed in order to modify the second-order, grid-level connectivity provided by PEGASUS. These modifications consist of two main aspects, domain decomposition and high-level connectivity.

The physical grids are first decomposed in an over-set manner for parallel implementation. For notational purposes, the grid elements generated due to geometric or resolution requirements are referred to as "grids", while elements resulting from the decomposition of grids for parallel processing are referred to as "blocks". Communication between blocks is handled though finite-sized overlaps consisting of coincident grid points (see Reference 12 for additional details). Each block is currently assigned to a single, unique processor. BELLERO handles finding the point-to-point connectivity data between blocks on the same grid, as well as decomposing the grid-level connectivity data provided by PEGASUS down to the block level.

BELLERO also modifies the original connectivity data to calculate high-order interpolation offsets and interpolation coefficients using the second-order values provided by PEGASUS as input. These high-order values are used in a general, three-dimensional, explicit interpolation formula

$$\overline{\phi}_p = \sum_{i,j,k=0}^{\sigma-1} R_k^{\zeta}\left(\Delta_{\zeta}\right)\cdot R_j^{\eta}\left(\Delta_{\eta}\right)\cdot R_i^{\xi}\left(\Delta_{\xi}\right)\cdot \phi_{I_p+i,J_p+j,K_p+k} \quad (1)$$

that yields the interpolated primitive flowfield variable $\overline{\phi}_p$ at an interpolation point p using the known functional values φ at a set of donating stencil points based on the donor point (I_p,J_p,K_p). The interpolation offsets, given by $(\Delta_\xi, \Delta_\eta, \Delta_\zeta)$, represent the distance from the base donor point (I_p,J_p,K_p) to the interpolation point in the computational space of the donor grid. The parameter σ is the formal order-of-accuracy of the interpolation method, and also equals the number of stencil points in each coordinate direction. The interpolation coefficients are found from the analytical expression

$$R_n^x = \frac{(-1)^{\sigma+n-1}}{\left[\sigma-(n-1)!\right]n!}\prod_{\substack{i=0\\ i\neq j}}^{\sigma-1}\left(\Delta_x - i\right) \quad (2)$$

In addition to the above modifications to the connectivity data, BELLERO performs two other important functions; hole management and boundary condition decomposition. Boundary condition decomposition simply involves decomposing the boundary conditions from the grid level to the block level.

Hole-cutting, or blanking, is incorporated into the algorithm by decoupling the points located inside a hole from the field points outside of the hold in the implicit spatial algorithm. Then the centered differencing and filtering formulations are replaced with their appropriate one-sided counterparts at the hole boundaries[13]. BELLERO identifies and tags these hole points for each coordinate direction so the one-sided formulations may be properly applied.

3. Low Sweep Delta Wing Computations

Low sweep delta-like wings are a common feature in the design of current and proposed UCAVs. The first results presented are for a 50° sweep delta wing, Figure 1, which corresponds to the experimental configuration investigated by Gursul and Wang[14]. Computations are performed for the same conditions as in the experiment, $\alpha = 15°$ and $Re = 2 \times 10^5$ and $Re = 6.2 \times 10^5$. The effect of mesh resolution on the numerical results for $Re = 6.2 \times 10^5$ and comparisons with the experimental measurements for $Re = 2 \times 10^5$ and 6.2×10^5 are made to validate the computational results.

3.1. Grid Resolution Study

Two different grids were developed for the present computations assuming flow symmetry to reduce computational requirements. The coarser H-O mesh consists of 268 points in the axial direction (171 located on the wing), 231 points in the circumferential direction and 183 points normal to the wing. A refined mesh of $442 \times 361 \times 219$ grid points was also developed. The objectives of this mesh refinement were to significantly decrease the mesh spacing in the axial direction and in the spanwise direction in the core of the vortex. The axial spacing on the wing and the spanwise spacing in the vortex core at the trailing edge were halved.

Figure 2 demonstrates the impact of mesh refinement on the global structure of the vortex for both the mean (Figure 2a) and instantaneous (Figure 2b) flow. Isosurfaces of constant axial vorticity colored by density contours highlight the general vortex structure. The fine grid solution captures smaller scale unsteady features of the vortical flow (Figure 2b) both in the shear layer that separates from the leading edge and rolls up to form the vortex as well as in the core of the vortex downstream of breakdown. As a result the mean flow exhibits more clear-cut, small-scale substructures in the outer shear layer and in the breakdown region downstream.

The effect of grid refinement on the computed flowfield can be further understood by examining the structure in planes normal to the vortex core as shown in Figure 1. Figures 3a and b compare the vortex structure upstream of breakdown at a location $\bar{x} = 0.1429$. On each mesh primary, secondary and tertiary vortices are observed, as well as a second vortex of the same sign as the primary vortex outboard near the leading edge. This type of dual vortex system has been observed previously for low sweep delta wings[15–17] and results from the interaction of the secondary flow with the primary shear layer. Increased unsteadiness resulting in significantly higher levels of turbulent kinetic energy is obtained with refinement, Figure 3c. Enhancement of the boundary-layer eruptive behavior induced by the vortex surface interaction and the resulting wandering of the primary vortex core are responsible for this increase in the fluctuations. This type of unsteady behavior has been described in detail in previous references (15 and 18–20). The net result is increased turbulent dissipation which weakens the primary and secondary vortices (Figure 3a).

Downstream of breakdown, the fine grid solution exhibits a much more detailed flow structure with significantly smaller scales being captured, Figure 4. Both the mean and instantaneous flow on the fine grid show more small scale features in the outer shear layer that rolls up to form the vortex (Figures 4a and c), as well as in the vortex core itself. Enhanced interactions of these structures with the surface boundary layer are also seen as they move across the wing surface. The resulting turbulent kinetic energy levels are smaller on the fine mesh but the turbulent kinetic energy is more evenly distributed throughout the vortex core. This contrasts with the behavior observed upstream of breakdown.

The grid resolution study has shown that significantly more of the unsteady, fine scale features of the flow are captured on the fine mesh. These results demonstrate that sufficient grid resolution remains important for correctly modeling this type of transitional flow even with the higher-order computational method employed. Subsequent comparisons with experiments will only consider the solutions on the fine mesh.

3.2. Comparison with Experiment

Comparisons between the experimental particle image velocimetry (PIV) measurements and the computations are made for two Reynolds numbers, $Re = 2 \times 10^5$ and $Re = 6.2 \times 10^5$. This was accomplished by interpolating the computational results onto the PIV grid to provide an equivalent computational representation. Figure 5 compares the mean vorticity and velocity magnitude at the axial location $x = 0.2$ for $Re = 2 \times 10^5$. Good qualitative agreement is seen between the computation and the experiment with all the salient features in the experiment being reproduced in the computation. The computation produces a somewhat stronger vortex at this location (Figures 5a and c), with what appears to be a correspondingly enhanced secondary

flow. The mean velocity magnitude on a plane through the vortex core, Figure 6, also shows good agreement between computation and experiment with vortex breakdown occurring at approximately the same axial location. The computation exhibits a sharper delineation of the vortex breakdown than the experimental measurements. A comparison of the instantaneous velocity magnitude on the same plane (Figure 7), also displays a striking similarity between the computation and the experiment with the primary unsteady flow structures observed in the experiment reproduced in the computation.

Examination of the results in the crossflow plane at the higher Reynolds number, $Re = 6.2 \times 10^5$, also reveals good correlation between the PIV measurements and the computation (Figure 8). The computed and experimental mean velocity magnitude agrees particularly well (Figures 8c and d), while a slightly smaller vorticity magnitude is noted in the core of the computed primary vortex. Both the experiment and the computation in Figure 9 show a conically shaped region of low speed flow associated with vortex breakdown that penetrates approximately the same distance upstream with similar velocity levels. In between this region and the intact vortex core denoted by the high jetlike velocities lies a region over which the breakdown of the vortex occurs. This region is longer and has more complex structure in the computation. The initial breakdown of the vortex in the computations occurs slightly upstream of the experimental location.

The overall good agreement between the computation and experiment provides confidence that the ILES approach is properly capturing the relevant flow features for this separated delta wing flow at moderate Reynolds numbers. This provides the needed foundation to extend the application of this approach to a more geometrically complex configuration such as a UCAV.

4. UCAV Configuration

Computations are now performed for a realistic unmanned combat air vehicle configuration. This UCAV configuration is a tailless delta-wing configuration with a 47° leading-edge sweep, and a ±30° trailing-edge crank. The leading-edge radius is considered sharp (less than 0.03 percent of the mean aerodynamic chord), which fixes the separation locations, thus, limiting the sensitivity of the aerodynamic data to Reynolds number effects on separation location. The Mach number and Reynolds numbers of the computations shown here are 0.1 and 32,000, respectively. An experimentally mounted sting is also modeled.

An overset-grid topology consisting of 15 grids and approximately 12 million grid points was developed for the symmetric half-span UAV configuration. Views of the surface grids and the off-body volumetric grids are shown in Figure 10. The grid system represents a significant increase in complexity from geometries previously examined with the high-order, overset-grid approach, while still maintaining a fairly simple topology. The high-order, overset-grid method in conjunction with the ILES approach was used to simulate the flow over this UCAV configuration at angles-of-attack of 6° and 15°. The high-order, compact, sixth-order spatial algorithm was employed with a tenth-order filter ($\alpha_f = 0.4$). For comparison purposes, these computations were also being run with a standard second-order explicit compact differencing algorithm. All results shown here are instantaneous values obtained after advancing the code 12.0 characteristic times from an initial free-stream condition.

The computed vortex structure for both low (top) and high (bottom) angle-of-attack cases is illustrated by plotting isosurfaces of constant axial vorticity colored by density contours in Figures 11a and b, respectively. For $\alpha = 6°$ (Figure 11a), a relatively coherent vortex structure develops downstream of the apex of the wing and exhibits a dual vortex structure similar to that observed for the low sweep delta wing[15]. In contrast the high angle-of-attack case (Figure 11b), generates a large region of complex, highly-unsteady, vortical flow originating at the apex and covering the outer two-thirds of the wing. An additional region of vorticity is also seen near the centerline in both cases due to separation of the flow from the curved upper surface of the vehicle. This separated flow is more clearly seen in Figure 12a where contours of the y-component of vorticity are plotted on a spanwise plane near the centerline of the vehicle. The separation of the boundary layer from the surface and the subsequent onset of instabilities in the separated shear layer are observed towards the trailing edge.

The imprint of the vortical flowfield above the wing can be seen in the instantaneous pressures on the surface of the UCAV, Figures 13a and b. Low pressure regions under the leading-edge vortex are visible in both cases. For $\alpha = 6°$, Figure 13a, this low pressure region emerges downstream of the apex with the development of the vortical flow. Significantly lower pressures are obtained on the upstream half of the vehicle originating at the apex for the high angle-of-attack case (Figure 13b). On the downstream half of the wing, higher levels of pressure are recovered due to the breakdown of the vortical flow structure and the onset of a stalled flow region.

The impact of utilizing the high-order approach may be seen in Figures 12 and 14, which compare the high-order scheme (top) with the low-order scheme (bottom). For $\alpha = 15°$, the high-order scheme captures notably more of the relevant unsteady, fine-scale details of the separated vortical flowfield. This is particularly evident in Figures 14c and d where contours of vorticity on a

plane normal to the leading edge are plotted. Small-scale, vortical structures in the shear layer emanating from the leading edge and unsteady wake structures for this massively separated flow are lost with the low-order scheme. One of the impacts of scheme fidelity at the lower angle of attack is seen in Figures 12a and b, where the separation near the symmetry plane is visualized. The low-order solution separates further upstream with larger and more diffuse unsteady flow features. These results demonstrate the importance of high-order accuracy for capturing the relevant small scales present in these complex, unsteady, vortical flowfields.

5. Concluding Remarks

A high-order overset grid approach has been presented for ILES simulations of unmanned combat air vehicle configurations. Grid resolution studies demonstrated that mesh resolution remains important for correctly modeling these types of unsteady, vortical flows even with the higher-order computational method employed. Comparisons of computations with high-resolution PIV measurements have demonstrated the ability of the scheme to accurately capture the highly unsteady vortical flowfield over a low sweep delta wing typical of current and proposed UCAV configurations. The scheme was then applied to a generic UCAV configuration where the significant improvements obtained by the application of the high-order method were demonstrated. These computations represented the first high-order simulations for a UCAV configuration.

Systems Used

Aeronautical System Center HP Opteron Cluster and Altix BX2, Army High Performance Computing Research Center Cray X1, Naval Oceanographic Office IBM SP4

References

1. Morton, S.A., J. Forsythe, A. Mitchell, and D. Hajek, "Des and RANS Simulations of Delta Wing Vortical Flows." *AIAA-2002-0587*, January 2002.

2. Morton, S.A., "High Reynolds Number DES Simulations of Vortex Breakdown over a 70m Degree Delta Wing." *AIAA2003-4217*, June 2003.

3. Görtz, Stefan, "Detached-Eddy Simulations of a Full-Span Delta Wing at High Incidence." *AIAA-2003-4216*, June 2003.

4. Gaitonde, D.V. and M.R. Visbal, "High-Order Schemes for Navier-Stokes Equations: Algorithm and Implementation into FDL3DI." *Technical Report AFRL-VA-WP-TR-19983060*, Air Force Research Laboratory, Wright-Patterson AFB, 1998.

5. Gaitonde, D.V. and M.R. Visbal, "Further Development of a Navier-Stokes Solution Procedure Based on Higher-Order Formulas." *AIAA Paper 99-0557*, January 1999.

6. Visbal, M.R. and D.V. Gaitonde, "High-Order Accurate Methods for Complex Unsteady Subsonic Flows." *AIAA Journal*, 37(10), pp. 1231–1239, 1999.

7. Visbal, M.R. and D.V. Gaitonde, "On the Use of Higher-Order Finite-Difference Schemes on Curvilinear and Deforming Meshes." *Journal of Computational Physics*, 181, pp. 155–185, 2002.

8. Visbal, M.R. and R.E. Gordnier, "A High-Order Flow Solver for Deforming and Moving Meshes." *AIAA Paper 20002619*, June 2000.

9. Visbal, M.R., P.E. Morgan, and D.P. Rizzetta, "An Implicit les Approach Based on High-Order Compact Differencing and Filtering Schemes (invited)." *AIAA-2003-4098*, June 2003.

10. Suhs, Norman E., Stuart E. Rogers, and William E. Dietz, "Pegasus 5: An automated pre-processor for overset-grid CFD." *AIAA Paper 2002-3186*, AIAA 32nd Fluid Dynamics Meeting, St. Louis, MO, June 2002.

11. Sherer, Scott E., Miguel R. Visbal, and Marshall C. Galbraith, "Automated preprocessing tools for use with a high-order overset-grid algorithm." *AIAA Paper 2006-1147*, 2006.

12. Gaitonde, Datta V. and Miguel R. Visbal, "Padé-type higher-order boundary filters for the Navier-Stokes equations." *AIAA J.*, 38(11), pp. 2103–2112, 2000.

13. Sherer, Scott E. and James N. Scott, "High-order compact finite-difference methods on general overset grids." *J Comput. Phys.*, 210(2), pp. 459–496, 2005.

14. Gordnier, R.E., M.R. Visbal, I. Gursl, and Z. Wang, "Computational and Experimental Investigation of a Non-Slender Delta Wing." *AIAA-2007-0894*, 2007.

15. Gordnier, R.E. and M.R. Visbal, "Compact Difference Scheme Applied to Simulation of Low-Sweep Delta Wing Flow." *AIAA Journal*, 43(8), pp. 1744–1752, 2005.

16. Yaniktepe, B. and D. Rockwell, "Flow Structure on a Delta Wing of Low Sweep Angle. "*AIAA Journal*, 42(3), pp. 513–523, 2004.

17. Taylor, G.S., T. Schnorbus, and I. Gursul, "An Investigation of Vortex Flows over Low Sweep Delta Wings." *AIAA-2003-4021*, June 2003.

18. Gordnier, R.E. and M.R. Visbal, "Vortex Structure over a Delta Wing." *Journal of Aircraft*, 31(1), pp. 243–248, Jan–Feb. 1994.

19. Visbal, M.R. and R.E. Gordnier, "Origin of Computed Unsteadiness in the Shear Layer of Delta Wings." *Journal of Aircraft*, 32(5), pp. 1146–1148, 1995.

20. Gordnier, R.E. and M.R. Visbal, "Instabilities in the Shear Layer of Delta Wings." *AIAA-95-2281*, June 1995.

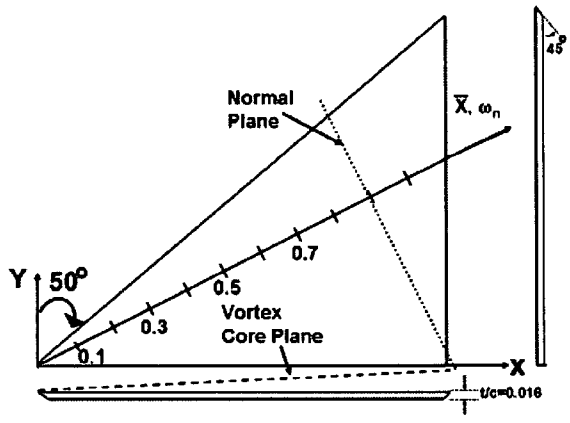

Figure 1. Computational delta wing geometry

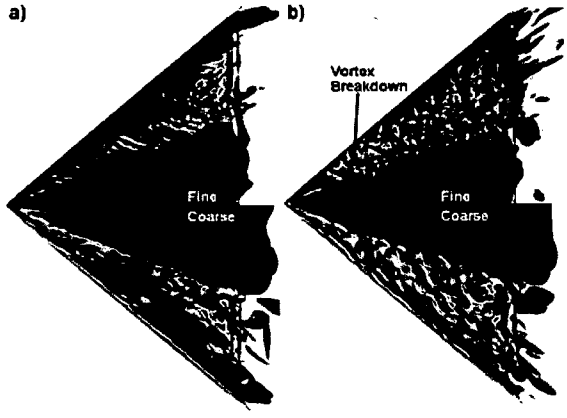

Figure 2. Isosurfaces of constant axial vorticity colored by density contours, $\alpha = 15°$, $Re = 6.2 \times 10^5$: a) mean vortex structure, b) instantaneous vortex structure

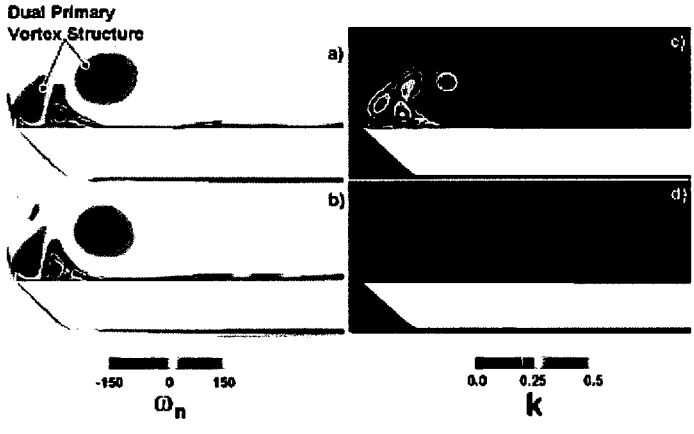

Figure 3. Contours of the mean axial vorticity and turbulent kinetic energy in a crossflow plane normal to the vortex, $\bar{x} = 0.1429$: a,c) Fine Mesh, b,d) Coarse Mesh

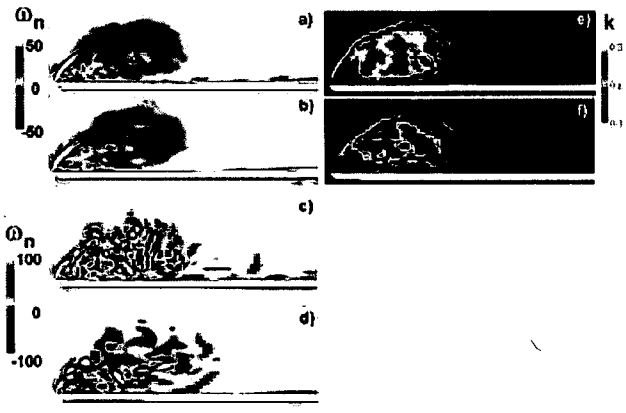

Figure 4. Contours of the mean(a,b) and instantaneous (c,d) axial vorticity and turbulent kinetic energy in a crossflow plane normal to the vortex, $\bar{x} = 0.85$: (a,c,e) Fine Mesh, (b,d,f) Coarse Mesh

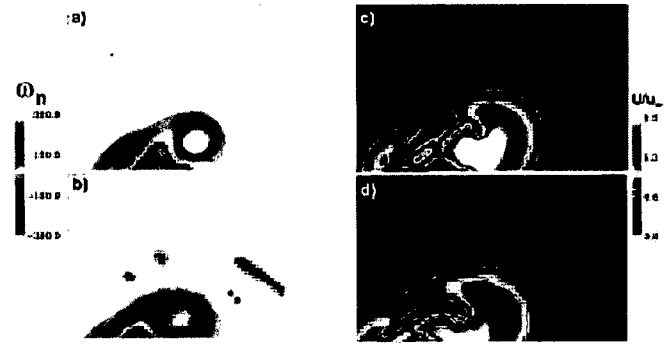

Figure 5. Comparison between the computation (a,c) and PIV measurements (b,d) on the crossflow plane x = 0.2: (a,b) mean vorticity and (c,d) mean crossflow velocity magnitude, $Re = 2 \times 10^5$

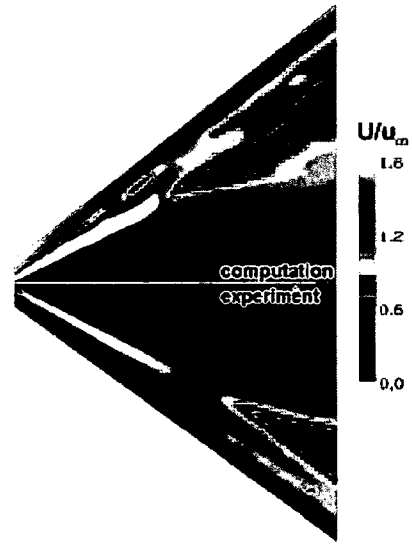

Figure 6. Comparison of Experimental and Computational mean velocity magnitude on a plane through the vortex core, $Re = 2 \times 10^5$

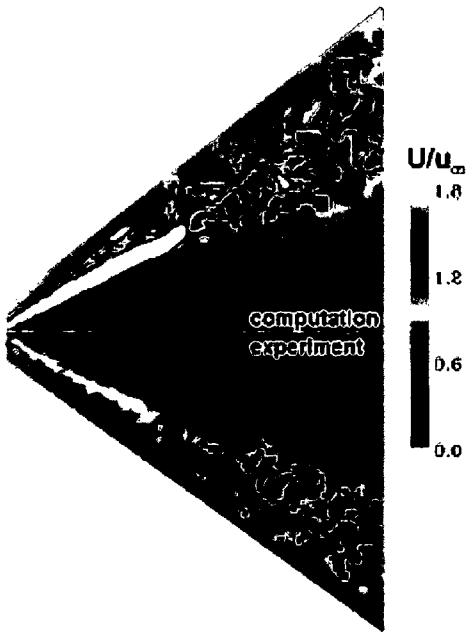

Figure 7. Comparison of Experimental and Computational instantaneous velocity magnitude on a plane through the vortex core, $Re = 2 \times 10^5$

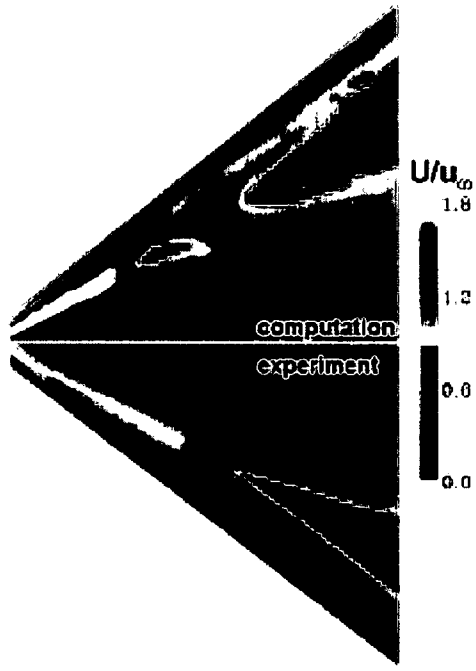

Figure 9. Comparison of Experimental and Computational mean velocity magnitude on a plane through the vortex core, $Re = 6.2 \times 10^5$

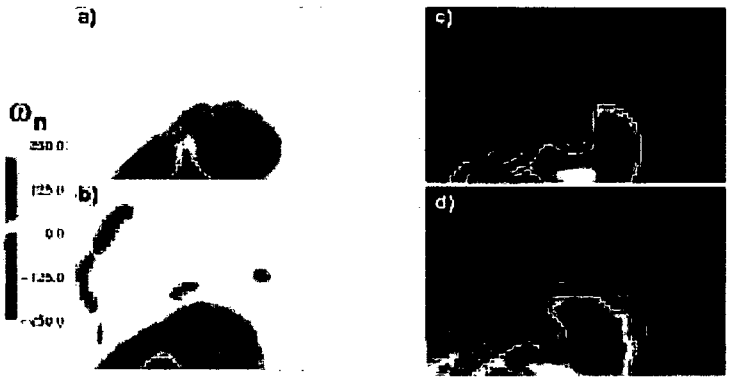

Figure 8. Comparison between the computation (a,c) and PIV measurements (b,d) on the crossflow plane $x/c = 0.2$: (a,b) mean vorticity, (c,d) mean crossflow velocity magnitude, $Re = 6.2 \times 10^5$

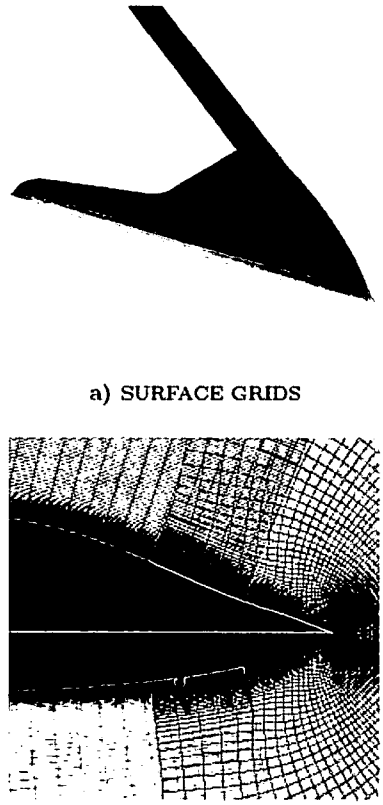

a) SURFACE GRIDS

b) OFF-BODY GRIDS IN LEADING EDGE REGION

Figure 10. Overset grid topology for UCAV computations

Figure 11. Isosurfaces of axial vorticity component for high-order UCAV simulation at two angles-of-attack: a) $\alpha = 6°$, b) $\alpha = 15°$

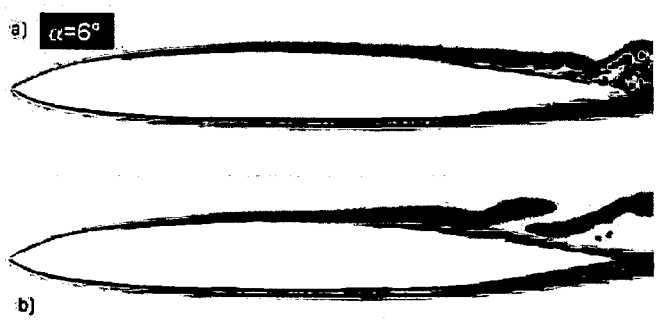

Figure 12. Contours of y-component of vorticity on a spanwise plane y=0.16: a) Sixth-Order Scheme, b) Second-Order Scheme

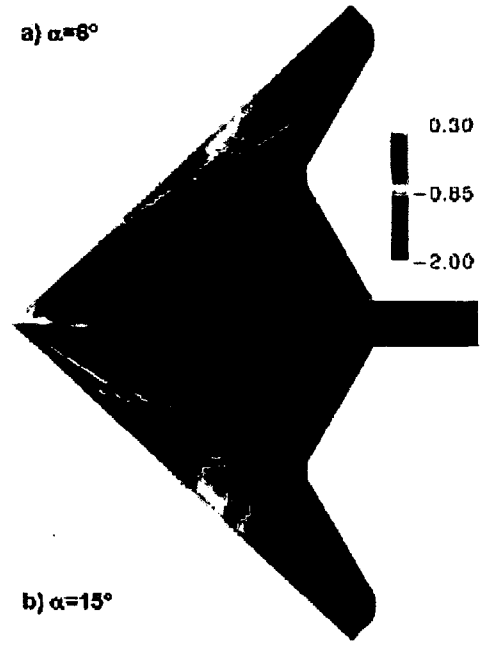

Figure 13. Instantaneous surface pressures on UCAV at two angles-of-attack

Figure 14. Isosurfaces of axial vorticity component for high angle-of-attack UCAV simulation ($\alpha = 15°$): (a,c) sixth-order simulation, b,d) second-order simulation